THE JOURNAL OF PHYSICAL CHEMISTRY C
A JOURNAL OF THE AMERICAN CHEMICAL SOCIETY

pubs.acs.org/JPCC

Article

Size-Dependent Response of CdSe Quantum Dots to Hydrostatic Pressure

Zifei Chen, J. Curtis Beimborn, II, Nicholas Kirkwood, Salvy P. Russo, J. Mathias Weber, and Paul Mulvaney*

Cite This: *J. Phys. Chem. C* 2023, 127, 8657−8669

Read Online

ACCESS | Metrics & More | Article Recommendations | Supporting Information

ABSTRACT: The size-dependent pressure response of oleate-stabilized CdSe quantum dots (QDs) in paraffin is investigated using diamond anvil cell experiments and density functional theory (DFT). For QDs above 3.0 nm, the photoluminescence shows a blue-shift of around 43 meV/GPa, close to the value for bulk CdSe, but the shift increases strongly for nanocrystals less than 3 nm in size. Conversely, the absorption shift is 45 meV/GPa above 3.0 nm but weakens to 35 meV/GPa for particles 1.5 nm in size. No crystallographic phase transitions occur below 2 GPa, and the optical effects are reversible. DFT calculations confirm that shifts in the bulk modulus begin for sizes estimated to be 1/2 of the Bohr radius, which we term the extreme confinement regime.

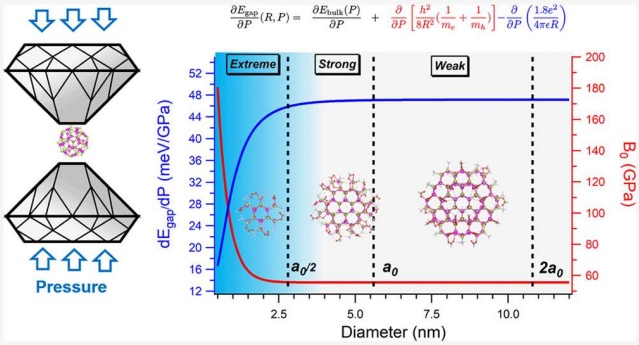

INTRODUCTION

Semiconductor nanocrystals (NCs) or colloidal quantum dots (QDs) have attracted enormous attention because of their size tunable optical properties. Their mechanical properties are similarly intriguing, but many fundamental questions in this context have still not been settled. There has been speculation that materials at the nanoscale may become harder or stronger than in the bulk due to the presence of fewer grain boundaries and dislocations.[1,2] Conversely, other studies have suggested that because of their large surface free energy, nanocrystals will ultimately exhibit weaker mechanical strength than the corresponding bulk phases.[3] An important step is to identify methods for carrying out quantitative mechanical measurements on dispersed nanocrystals. To date, most studies have exploited atomic force microscopy (AFM) or other scanning probe techniques to infer the mechanical response of single nanocrystals.[4−12] These are complicated by the presence of the substrate, the difficulty of applying a well-defined mechanical stress to the particle, the complications due to variations in AFM tip shape, and the large number of individual experiments necessary to ensure statistical validity.

A different approach is to investigate the response of nanocrystals to high pressure in concert with optical spectroscopy to deduce the mechanical properties. (High pressure here means hydrostatic loading.) Such measurements have the advantage of offering ensemble results, which are more statistically relevant, but this in turn relies on the samples being homogeneous in size and shape.

The challenge is to connect the changes in optical spectra to the mechanical properties of the nanocrystal. In the case of gold nanocrystals, the Drude model provides a simple explanation for shifts in the surface plasmon resonance under pressure. This enables the bulk modulus of metallic gold nanocrystals to be determined optically.[13−15] In the case of semiconductor materials, the origins of pressure-induced spectral changes are more complex. For example, some semiconductors such as PbS exhibit a red-shift under pressure, while others such as CdS and CdSe exhibit a blue-shift. Pioneering studies were performed by Drickamer and colleagues in the 1960s. These revealed a number of striking changes to the optical properties of semiconductors, including shifts of the luminescence spectrum and the absorption edge. In some cases phase changes were also identified.[16]

Hydrostatic loading of CdSe nanocrystals was first reported by the Alivisatos group in 1993.[17] These studies focused on size-dependent phase changes, in particular the formation of rock-salt CdSe. This phase change resulted in complete loss of photoluminescence (PL) but was reversible. Other important effects have been identified including high-order phase transitions[18−21] and the formation of new phases,[22,23] as well as phase transformation into more thermodynamically stable structures.[24,25] There have been subsequent high-pressure QD investigations reported for CdSe,[26−30] core/shell CdSe nano-

Received: February 26, 2023
Revised: April 16, 2023
Published: May 1, 2023

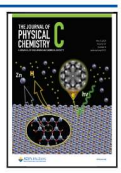

https://doi.org/10.1021/acs.jpcc.3c00998
J. Phys. Chem. C 2023, 127, 8657−8669

particles,[31] and PbSe.[32] More recently, Weber et al. reported the high-pressure behavior of $CsPbBr_3$ perovskite NCs with different sizes.[33] To date, however, a systematic study to uncover the actual size dependence of the bulk modulus has not been undertaken, nor have there been any tests for the limit of applicability of bulk band structure concepts to the mechanics of nanocrystals.

Compared to sophisticated bulk system simulation techniques, the theory of the pressure dependence of the ground states and excited states of colloidal QDs is not well established, although several models have been proposed including direct atomistic simulations and continuum theories,[34,35] empirical force field and coarse-grained models,[36,37] and some first-principle calculations for smaller particles.[27,38,39]

A key limitation in earlier studies has been the widely used bulk approximation and use of the hydrogen/pseudo-hydrogen passivation technique.[38] This does not reflect the real surface chemistry of colloidal quantum dots; e.g., it does not include surface reconstruction or ligand−core interactions and thus fails to reproduce physical observables, particularly the excited-state energies of the system. In spectacular cases, density functional theory (DFT) calculations of H-passivated semiconductor NCs even predict zero band gaps and metallic behavior![40] Although pseudo-hydrogen techniques can partially solve this, they still do not address the effects of charge transfer and rehybridization at the QD surface.[41]

In this work, we have performed extensive experimental measurements on CdSe nanocrystals in diamond anvil cells and combined these with a theoretical investigation of the bulk modulus over a wide range of sizes. DFT has been employed to investigate the pressure coefficient and bulk modulus as a function of CdSe quantum dot size. Instead of hydrogen/pseudo-hydrogen ligation, we have adopted ammonia/carboxylate ligands as the passivants to better represent the colloid surface chemistry. In particular, the regime below the conventional "strong quantum confinement limit" will be discussed. We will show there is good evidence for the existence of a second size regime, which occurs for QDs smaller than around half of the Bohr radius, i.e., $a_0/2$, where there is a transition in mechanical behavior.

THEORY

Pressure-Dependent Brus Equation. To understand the energy gap shift at different applied hydrostatic pressures, we first revisit the expression derived by Brus,[42,43] which depicts the relationship between the nanocrystal size and the electronic structure of the semiconductor.

$$E_{gap} = E_{bulk} + \frac{h^2}{8R^2}\left(\frac{1}{m_e} + \frac{1}{m_h}\right) - \frac{1.8e^2}{4\pi\epsilon R} \tag{1}$$

Here R stands for nanocrystal radius, E_{gap} is the optical band gap of quantum dots of a given radius, E_{bulk} is the energy gap of the respective bulk material, which is independent of particle size, m_e and m_h are the effective masses of electrons and holes, respectively, and $\epsilon = \epsilon_r\epsilon_0$ is the dielectric constant consisting of the permittivity of vacuum (ϵ_0) and the relative permittivity of the solvent (ϵ_r).

The second term on the right-hand side (RHS) of eq 1 represents the additional energy due to quantum confinement, which has a R^{-2} dependence on the band gap energy. The third term quantifies the Coulomb interaction in an exciton and has a R^{-1} scaling. This is sometimes neglected in high dielectric environments. If the electron−hole spatial correlation effects are to be considered,[44] then a Rydberg energy term ($E \times Ry$) could be added, but it will not be discussed in our case for simplicity.

Under hydrostatic loading, the work by Drickamer has shown that there is a well-defined optical shift in the band edge of the bulk semiconductor.[16] Hence, the first term on the RHS of eq 1 can be written more generally as

$$E_{bulk}(P) = E_{bulk}(0) + \alpha_0 P + \beta_0 P^2 \tag{2}$$

where α_0 and β_0 are the first- and second-order pressure coefficients of the bulk material, respectively. The corresponding values for QDs with arbitrary sizes are denoted by α and β, respectively, and are functions of the particle size R.

Together, the second and third terms on the RHS of eq 1 are written as $E^c_{gap}(P)$, and they represent the quantum confinement contribution to the energy gap, and this is expected to be pressure dependent. To investigate this more closely, we take the derivative of $E^c_{gap}(P)$ with respect to the pressure and apply the chain rule:

$$\frac{\partial E^c_{gap}(R,P)}{\partial P} = \frac{\partial E^c_{gap}(R,P)}{\partial R}\frac{\partial R}{\partial V}\frac{\partial V}{\partial P} \tag{3}$$

$$\frac{\partial E_{gap}}{\partial P}(R,P) = \frac{\partial E_{bulk}(P)}{\partial P} + \frac{\partial}{\partial P}\left[\frac{h^2}{8R^2}\left(\frac{1}{m_e} + \frac{1}{m_h}\right)\right] - \frac{\partial}{\partial P}\left(\frac{1.8e^2}{4\pi\epsilon R}\right) \tag{4}$$

The first term on the RHS of eq 4 can be obtained from eq 2, leading to $\alpha_0 + 2P\beta_0$. To evaluate the second and third terms in eq 4, we note that if there is no dependence on particle size R, of the effective masses m_e and m_h and dielectric constant ϵ, then these two terms vanish, which leads to

$$\frac{\partial E_{gap}(R,P)}{\partial P} = \alpha_0 + 2\beta_0 P \tag{5}$$

Equation 5 does not explicitly include a size term, which means the optical shift is size-independent in this case and is the same as the bulk value. However, generally speaking, all quantities in the second and third terms of eq 4 need to be considered as functions of hydrostatic pressure. For example, the relationship between radius and pressure can be understood from Murnaghan's equation

$$V = V_0\left(1 + P\frac{B_0'}{B_0}\right)^{-1/B_0'} \tag{6}$$

where B_0 is the bulk modulus, B_0' is the first derivative of B_0 with respect to pressure, and V_0 is the volume of the reference state (i.e., in the equilibrium geometry). Differentiating V with respect to P, expanding the result into a Taylor series at $P = 0$, and retaining terms up to second order yields

$$\frac{\partial V}{\partial P} = -\frac{V_0}{B_0'}\left(1 + P\frac{B_0'}{B_0}\right)^{-1/B_0'-1}\left(\frac{B_0'}{B_0} - P\left(\frac{B_0'}{B_0}\right)^2\right)$$

$$= -\frac{V_0}{B_0} + \frac{1 + 2B_0'}{B_0^2}V_0 P + O(P^2) \tag{7}$$

https://doi.org/10.1021/acs.jpcc.3c00998
J. Phys. Chem. C 2023, 127, 8657−8669

Here $O(P)^2$ refers to terms of order P^2 and $\partial B_0/\partial P = B_0'$ and $\partial B_0'/\partial P = 0$ because only the linear term of P is important here. Assuming the particles are spherical, i.e., $V = {}^4/_3\pi R^3$, we can explicitly evaluate the second and third terms in eq 4

$$\frac{\partial}{\partial P}\left[\frac{h^2}{8R^2}\left(\frac{1}{m_e}+\frac{1}{m_h}\right)\right] = \frac{V_0}{16B_0\pi}\left[\frac{h^2}{R^5}\left(\frac{1}{m_e}+\frac{1}{m_h}\right)\right] + \frac{h^2}{8R^2}\frac{\partial}{\partial P}\left(\frac{1}{m_e}+\frac{1}{m_h}\right) + O(P)$$

$$-\frac{\partial}{\partial P}\left(\frac{1.8e^2}{4\pi\varepsilon R}\right) = -\frac{V_0}{16\pi^2 B_0\varepsilon}\frac{1.8e^2}{R^4} - \frac{1.8e^2}{4\pi R}\frac{\partial}{\partial P}\frac{1}{\varepsilon} + O(P) \tag{8}$$

Because we are only interested in the first derivative of the pressure, $-V_0/B_0$ is the leading term in eq 7. We can put all quantities higher than first order in P into $O(P)$—these make no contribution to the first pressure coefficient.

After substituting eq 8 into eq 4, the final expression for the pressure coefficient is

$$\frac{dE_{gap}}{dP} = \underbrace{\left\{\alpha_0 + \frac{V_0(\{R\})}{16B_0\pi}\left[\frac{h^2}{R^5}\left(\frac{1}{m_e}+\frac{1}{m_h}\right)\right] - \frac{V_0}{16\pi^2 B_0\varepsilon}\frac{1.8e^2}{R^4}\right\}}_{\mathcal{D}} + \underbrace{\left[\frac{h^2}{8R^2}\frac{\partial}{\partial P}\left(\frac{1}{m_e}+\frac{1}{m_h}\right) - \frac{1.8e^2}{4\pi R}\frac{\partial}{\partial P}\frac{1}{\varepsilon}\right]}_{\mathcal{U}} + O(P) \tag{9}$$

Here $\mathcal{D}$ stands for the well-defined leading term of the pressure dependence, and $\mathcal{U}$ represents the undetermined contribution from the changes in the effective masses of the charge carriers and dielectric constant with respect to pressure.

It should be noted that the bulk modulus B_0 and dielectric constant ϵ in the $\mathcal{D}$ term are treated as constants, which is only valid in the large size limit, and $V_0(\{R\})$ is the reference volume, which depends parametrically on the particle size. For instance, one scaling relation is given by Cohen[38,45] to describe the size dependence of the bulk modulus. The term $\mathcal{U}$ can be neglected only in the large size regime. Conversely, in the ultrasmall size regime, there is a significant contribution from the electron kinetic energies, and the effective mass approximation breaks down.

We now look at the behavior of $\frac{dE_{gap}}{dP}$ in the large size limit ($R \to \infty$). When $R \to \infty$, the $\mathcal{D}$ term in eq 9 approaches α_0, which is as expected because all properties should approach the bulk values in the thermodynamic limit of large sizes.

Given that both the band gap and $\frac{dE_{gap}}{dP}$ will converge to their bulk values, their asymptotic behavior is of interest; i.e., how fast do they reach the bulk limit? We define two increments

$$f(R) = \frac{h^2}{8R^2}\left(\frac{1}{m_e}+\frac{1}{m_h}\right) - \frac{1.8e^2}{4\pi\varepsilon R}$$

$$g(R) = \frac{V_0}{16B_0\pi}\left[\frac{h^2}{R^5}\left(\frac{1}{m_e}+\frac{1}{m_h}\right)\right] - \frac{V_0}{16\pi^2 B_0\varepsilon}\frac{1.8e^2}{R^4} \tag{10}$$

where $f(R)$ represents the changing behavior of the band gap with respect to particle size, and $g(R)$ is the main contribution to $\frac{dE_{gap}}{dP}$ when approaching bulk values. Considering the ratio $f(R)/g(R)$ in the $R \to \infty$ limit yields

$$\left.\frac{f(R)}{g(R)}\right|_{R\to\infty} \to \infty \tag{11}$$

Equation 11 indicates that the convergence of $\frac{dE_{gap}}{dP}$ is faster than that of E_{gap} in the large size limit. Conversely, in the small size regime, because of the complexity of eq 4, we will use DFT to investigate several standard systems.

Equations of State. The Brus equation provides an analytical solution for the dependence of the optical band gap on particle size. To understand the pressure response of realistic systems, an equation of state (EOS) is needed to link the energy or pressure to the material volume. The pressure−volume EOS was first treated by Murnaghan.[46] Birch extended this theory and developed what is nowadays termed the Birch−Murnaghan EOS.[47] The third-order Birch−Murnaghan (BM) equations of state can be written as

$$E(V) = E_0 + \frac{9V_0B_0}{16}\left\{\left[\left(\frac{V_0}{V}\right)^{2/3} - 1\right]^3 B_0' + \left[\left(\frac{V_0}{V}\right)^{2/3} - 1\right]^2 \times \left[6 - 4\left(\frac{V_0}{V}\right)^{2/3}\right]\right\} \tag{12}$$

$$P(V) = \frac{3B_0}{2}\left[\left(\frac{V_0}{V}\right)^{7/3} - \left(\frac{V_0}{V}\right)^{5/3}\right]\left\{1 + \frac{3}{4}(B_0' - 4) \times \left[\left(\frac{V_0}{V}\right)^{2/3} - 1\right]\right\} \tag{13}$$

The definitions of B_0, B_0', and V_0 are the same as eq 6, while E_0 is the energy of the reference state. Equations 12 and 13 will be used to analyze the DFT data in this study.

EXPERIMENTAL DETAILS.

Chemicals. Cadmium oxide (CdO, Aldrich, 99.99%), selenium powder (Aldrich, 99.9%), oleic acid (OA, Aldrich, 90%), trioctylphosphine (TOP, Aldrich, 90%), 1-octadecene (ODE, Aldrich, 90%), oleylamine (Pfaltz and Bauer Inc., 97%), hexadecylamine (HDA, Merck, synthesis grade), and bis(2,2,4-trimethylpentyl)phosphinic acid (TMPPA, Cytec Specialty Chemicals) were used in the preparations described here. Hexane, chloroform, propanol, ethanol, and methanol were all of analytical grade and purchased from Univar. All chemicals and solvents were used without further purification.

Quantum Dot Synthesis. CdSe QDs with sizes larger than 2 nm were using the method reported by Van Embden et al. and Peng et al.[48,49] For instance, to synthesize QDs with 6.7 nm size, the following procedure was used: 0.06 g of CdO, 1.80 g of OA, and 12 g of ODE were mixed and heated at 80 °C

https://doi.org/10.1021/acs.jpcc.3c00998
J. Phys. Chem. C 2023, 127, 8657−8669

under vacuum and degassed for 30 min. The solution was then heated to 300 °C under nitrogen until the solution turned colorless. Then, 0.037 g of selenium powder in 1.16 g of TOP, mixed with 4.0 g of ODE and 0.250 g of TMPPA, was swiftly injected. The temperature was then allowed to drop to 240 °C for 80 min to allow the growth of the nanocrystals.

For sizes smaller than 2 nm, we applied the approach reported by Hens et al.[50] Typically, cadmium myristate (0.2 mmol), 0.6 mmol of HDA, and 10 mL of ODE were degassed for 1 h at 100 °C under a nitrogen flow in a 25 mL four-necked flask. The solution was subsequently heated to 245 °C under a nitrogen atmosphere. At this point, 2 mL of a 1 M TOPSe solution was swiftly injected, and the reaction temperature was held at 230 °C. Growth was conducted for 5 s and stopped by addition of 10 mL of solvent at 20 °C.

In all cases, the nanoparticles were precipitated by adding a 1:1−1:2 mixture of 2-propanol and methanol. The precipitate was separated by centrifugation and redissolved in paraffin in the presence of excess oleic acid.

High-Pressure Measurements. Hydrostatic pressure was generated in a gas membrane driven diamond anvil cell (DAC) with type Ia 16-sided diamond anvils (Diacell μ ScopeRT(G), diamond base diameter 2.5 mm, culet 0.50 mm, NA = 0.54), with details published elsewhere.[33,51] The sample volume was prepared by laser-drilling a hole with ca. 150 μm diameter into preindented type 302 stainless steel gaskets, and paraffin was used as the pressure transducing medium. Solutions of CdSe QDs in paraffin were placed into the sample volume together with a few grains of powder.

PL spectra were collected using a confocal microspectrometer (Horiba XploRa) under excitation by continuous-wave (CW) 532 nm (confocal) or 406 nm (wide field). For samples with d < 3 nm, we used 406 nm only. Exploratory measurements for the larger QDs employing both wavelengths independently showed that there was no significant change in the PL peak wavelength upon changing the excitation wavelength. The CdSe PL spectra were acquired using a 600 lines/mm grating affording 0.3 nm resolution. With confocal illumination, the laser intensity for collecting CdSe PL spectra was kept below 20 μW in a focal spot with a diameter of the order of several micrometers, while the intensity under wide-field illumination is 2 mW over a focal spot of hundreds of micrometers diameter. The PL peak energy was determined to within ±0.01 eV. Ruby fluorescence spectra were employed for pressure measurement, obtained with a 1800 lines/mm grating (0.1 nm resolution), and the R_1 line was used to calculate the pressure.[52] The errors in the pressure determination using this method are typically ±100 MPa in the pressure range of the current work. Several runs were acquired with most QD sizes, using fresh samples and gaskets for each run. Spectra were acquired until a pressure of 2 GPa to ensure the paraffin remained hydrostatic.[53]

A fiber-optic UV−vis spectrometer (Avantes AvaSpec-2048) was used to take optical absorption measurements on QD samples. Visible light from an Avantes AvaLight-HAL fiber optic light source was coupled into one input of a bifurcated multimode fiber (Avantes FCB-UVIR400-2), and a CW 532 nm laser (5 mW) was coupled into the second input of the fiber. The output of this fiber was then focused onto the sample region of the DAC using a matched achromatic lens pair (ThorLabs MAP1030100-A). The DAC was mounted on a three-axis micropositioning stage. The light exiting the other side of the DAC was collected with a second identical matched achromatic lens pair and coupled into a multimode fiber (Avantes FC-UV400-2) which was connected the AvaSpec-2048 fiber-optic spectrometer. A removable 550 long pass (LP) filter was installed between the lens pair and the fiber coupler to block the 532 nm excitation light while taking ruby fluorescence spectra. In order to take a reference spectrum before each experiment, a single ruby grain was selected and added to the DAC along with neat paraffin. The DAC along with the blank sample and ruby grain were placed in the setup and the position of the DAC was adjusted to maximize the transmission signal of the lamp spectrum through the gasket hole. This spectrum was recorded and saved to be used as the absorption measurement baseline. The position of the DAC was recorded by imaging the gasket hole with a camera through a stereo zoom microscope. This allowed the DAC to be returned to the exact position at which the reference spectrum was taken. The ambient pressure spectrum of the ruby grain was recorded by exciting it with the 532 nm laser with the 550 LP filter installed. The DAC was removed, and the QD suspension in paraffin was added to the DAC along with the same ruby grain from the reference measurement. Finally, the DAC was mounted on the setup again for high-pressure absorption experiments.

THEORETICAL MODELING

Models. To understand the changes in electronic levels of QDs induced by pressure, two representative systems, i.e., zinc-blende (ZB) tetrahedral CdSe QDs and wurtzite (WZ) spherical QDs, are considered. Cd dangling bonds and other trap states have a significant effect on the optical properties of II−VI QDs. In order to minimize the surface Cd trap states, the ligand passivation strategies should satisfy two rules: (1) charge neutrality (no net charge exists in terms of the ligand−core complex); (2) minimization of the Cd dangling bonds (each Cd atom is in four-coordinated sp^3 geometry).

The structures of zinc-blende CdSe clusters have been explored both experimentally and theoretically.[54,55] It has been shown that their cores tend to have pyramidal structures with Cd-rich {111} facets exposed. Their general stoichiometry is $Cd_{(x+1)(x+2)(x+3)/6}Se_{x(x+1)(x+2)/6}$, which can be abbreviated as T_x, where x represents the number of layers within the tetrahedral structures. Therefore, the ratio of Cd:Se is not exactly 1:1, and a number of Cd dangling bonds exist at the surface. To balance the extra charge of the core, X-type ligands (one-electron, donating ligands) are needed. Each additional Cd ion introduces two positive charges, so the number of X-type ligands required is $(x + 1)^2 + (x + 1)$. Furthermore, to reduce the number of dangling bonds to the greatest extent, we note that Cd atoms tend to maintain sp^3 tetrahedral geometry; i.e., the Cd atoms prefer to bond to 3, 2, and 1 ligands at vertices, edges, and facets, respectively. As a result, $(x + 1)^2 + (x + 1)$ more L-type ligands are required, which gives $Cd_{(x+1)(x+2)(x+3)/6}Se_{x(x+1)(x+2)/6}X_{(x+1)^2+(x+1)}L_{(x+1)^2+(x+1)}$ as the final chemical formula for T_x clusters. For simplification, we chose NH_3 as the L-type ligand and HCO_2^- as the X-type ligand in the DFT calculations. The models range from 1 to 5 layers, and one more 8-layer structure is used to model the largest possible QD within our computational limits.

Unlike zinc-blende CdSe, wurtzite CdSe QDs exhibit approximately spherical morphology, and the ratio of Cd:Se atoms is 1:1. Five stoichiometric, spherical QDs ($(CdSe)_y$, where y = 6, 15, 33, 45, and 66) are initially cut from bulk crystal, and one more structure $(CdSe)_{122}$ is generated as a

https://doi.org/10.1021/acs.jpcc.3c00998
J. Phys. Chem. C 2023, 127, 8657−8669

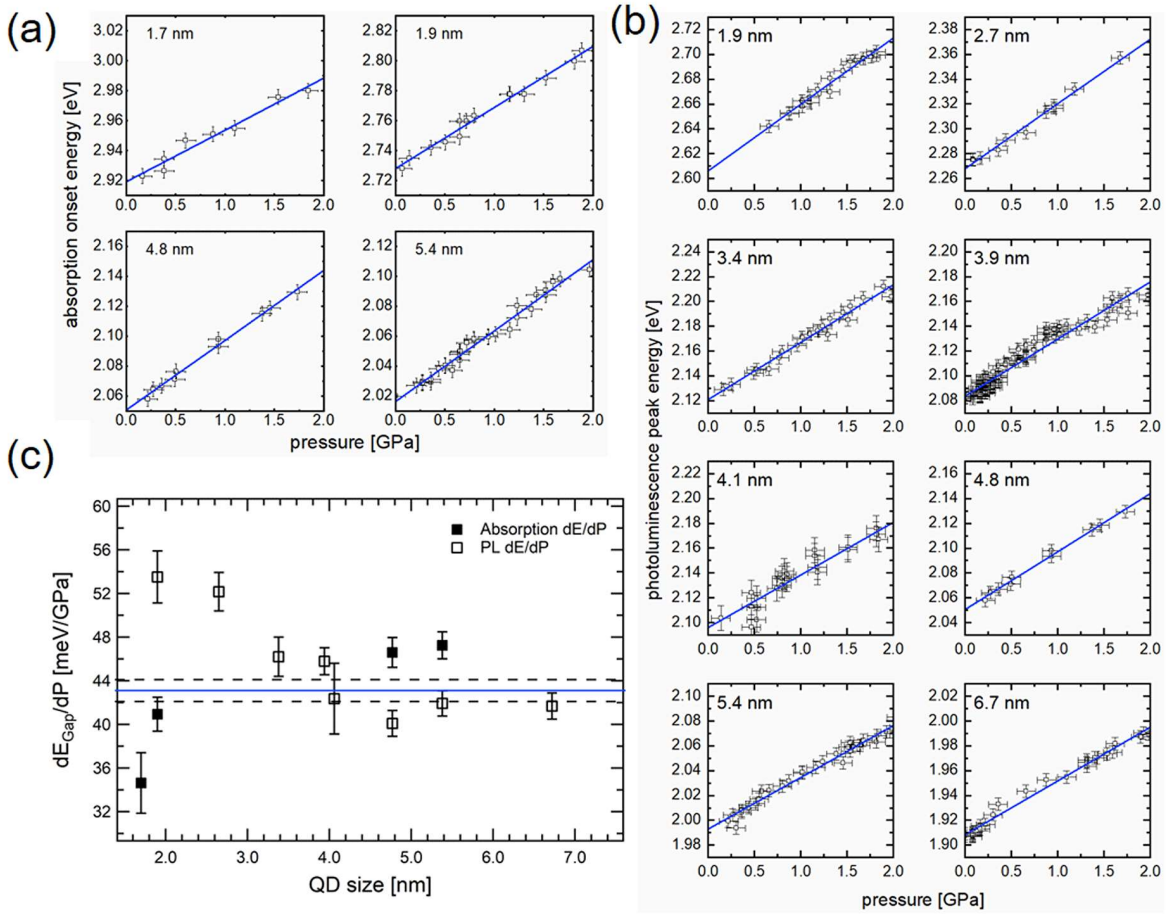

Figure 1. (a) Experimentally determined onset of absorption for wurtzite CdSe QDs as a function of the hydrostatic pressure for different QD sizes. (b) Experimentally determined emission peaks for wurtzite CdSe QDs as a function of the hydrostatic pressure for different QD sizes. Samples dispersed in paraffin with oleate ligands at room temperature. (c) Experimentally determined optical shifts vs pressure for different sized CdSe QDs determined from the absorption and emission spectra in (a) and (b). Horizontal lines represent the bulk behavior as reported by Haller et al.[71]

representative of medium-sized WZ QDs. Again the guiding principle is to reduce the number of Cd dangling bonds to the maximum extent. As a result, all of the Cd atoms in these initial structures possess only one or two dangling bonds, and the whole structure is approximately spherical. To deal with the WZ passivation problem in our models, one NH_3 is employed to passivate the Cd atoms with one dangling bond, while one NH_3 ligand and one HCO_2^- ligand are used to saturate Cd atoms with two dangling bonds. The introduction of carboxylate ligands will break charge neutrality. To address this, extra protons are connected to surface Se atoms. Unlike ZB QDs, the surface of the WZ structure is neither Cd- nor Se-rich. Thus, ideally all cadmium traps are fully eliminated while some selenium defects potentially still exist at the WZ QD surfaces.

Computational Details. DFT and its time-dependent extension (TD-DFT) are used to obtain the ground- and excited-state properties of CdSe QDs, respectively. It has been established that inclusion of spin−orbit coupling is not necessary to obtain the correct electronic structures and dE_{gap}/dP if the ligand effects are properly considered[39] and that DFT tends to miscalculate the band gap energy but provides an accurate representation of the pressure dependence.[56,57] All geometries are fully optimized using the PBE0 hybrid functional[58] for smaller QDs (i.e., ZB-T_x, x = 1, 5 and WZ-$(CdSe)_y$, y = 6, 15, 33, 45, 66) at T = 0 K using the TURBOMOLE software package,[59] which has been reported to well describe the ground- and excited-state behavior for similar systems.[54,60,61] Double-ζ basis sets def2-SV(P) are applied for both Cd and Se atoms. The effective core potential (ECP) approximation for Cd atoms is used for atomic orbitals below the 3d/3p shell. Also, all-electron basis sets def2-SV(P) are applied to ligand atoms. For medium-sized QDs, i.e., ZB-T_8 and WZ-$(CdSe)_{122}$, the geometry optimizations are computed using the QUICKSTEP codebase within CP2K.[62,63] The Gaussian augmented plane-wave method (GAPW) method[64] is employed for electronic structure calculations with an energy cutoff of 520 Ry, with the Perdew−Burke−Ernzerhof (PBE) generalized gradient approximation density functional,[65] using the Goedecker−Teter−Hutter (GTH) pseudopotential[66] within the double-ζ valence-polarized molecular optimized (DZVP-MOLOPT-SR-GTH) basis set[67] with an energy convergence and atomic force criterion of 10^{-6} hartree and 4.5×10^{-4} hartree/bohr. The $6 \times 6 \times 6$ unit cells are calculated with periodic boundary conditions, and the Γ point is used to sample the Brillouin zone due to the large super cell. The TD-DFT excited-state calculations of all structures are performed with PBE0.[58,68] Because only relative energies need to be compared, all the geometry optimization and excited-state calculations are performed in the gas phase. More discussions about functional selections can be found in Figure S1.

https://doi.org/10.1021/acs.jpcc.3c00998
J. Phys. Chem. C 2023, 127, 8657−8669

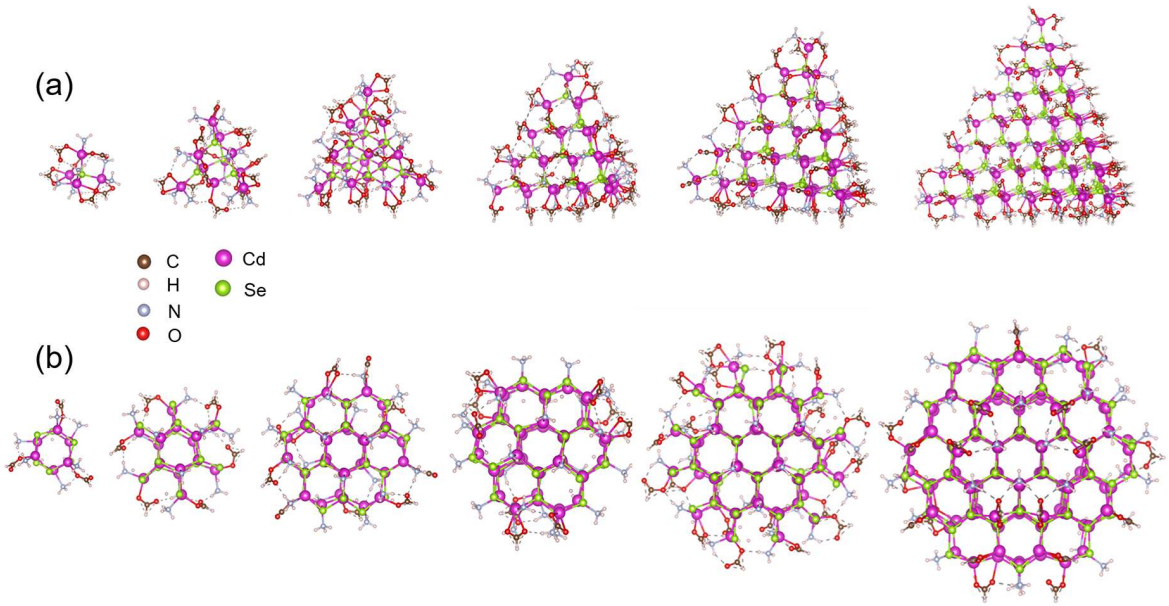

Figure 2. Structures of CdSe CQDs with different sizes: (a) zinc-blende tetrahedral structures with different layers T_x, where x = 1 to 5, and 8; (b) wurtzite sphere-like structures $(CdSe)_y$, y = 6, 15, 33, 45, 66, and 122. The ZB QDs are passivated by just X = $HCOO^-$ and L = NH_3 ligands, whereas the WZ QDs are passivated by $HCOO^-$ and NH_3 ligands but with additional H^+ ions to maintain electroneutrality of the clusters. These protons are placed close to the surface Se atoms.

In order to understand the QD mechanical and optical properties under hydrostatic pressure, the DFT calculations are performed for uniformly contracted QDs, assuming no phase transformation occur during this process. It should be noted that although the bulk modulus tensor is in general an anisotropic property, we have utilized an isotropic scalar approximation for simplification. The compressed structures are generated from the fully optimized ground-state structures. The gap between the lowest unoccupied molecular orbital (LUMO) and the highest occupied molecular orbital (HOMO) of the quantum dots is approximated by using the energy differences between the lowest virtual orbital and highest occupied Kohn−Sham orbitals. For ligand passivated cluster calculations, we use constrained optimization strategies; i.e., we compress the inorganic core structures uniformly but leave the ligands free to optimize. The volume of the CdSe core is estimated by implementing the Convex hull algorithm in MATLAB.[69] The molecular orbital analysis has been performed using the Multiwfn software.[70]

RESULTS AND DISCUSSION

Diamond Anvil Experiments. To verify the predictions from the Theory section, we have employed diamond anvil experiments to measure the absorption and emission spectra of CdSe QDs with different radii under hydrostatic pressures up to 2 GPa. Representative experimental first exciton peaks from absorption and PL of CdSe QDs of different sizes are shown as a function of hydrostatic pressure in Figure 1a,b.

Wurtzite CdSe QDs exhibit size-dependent optical spectra, and as the size decreases, there is a systematic blue-shift in both absorption and PL. When a hydrostatic pressure up to 2 GPa is applied, the excitation and emission energies of all QDs shift monotonically toward higher energies, as evident in Figure 1. When the pressure is released, the spectra shift back to lower energies, with no evidence for hysteresis, indicating that the process is reversible. Because of the nonhydrostatic behavior of paraffin above 2 GPa (see ref 53), only the low-pressure regime will be discussed in the present work.

The pressure coefficients α determined from the absorption and PL spectral measurements are summarized in Figure 1c. Above 3.0 nm in diameter, the pressure coefficient approaches the bulk values reported by Haller et al. (43 meV/GPa)[71] and by Drickamer of 37 meV/GPa.[72] We conclude that in the usual quantum size regime below the bulk exciton radius of 5.6 nm, the pressure coefficient is more or less the same as bulk and independent of QD size. For significantly smaller sizes, less than around half the bulk exciton radius, the PL pressure coefficient increases with decreasing size and becomes size dependent.

Curiously, the values of the pressure coefficients for absorption and PL deviate from each other below about 3.0 nm. The absorption shift becomes smaller than for bulk crystals, while the PL shift becomes larger.[71−74] This behavior is in accord with our theoretical predictions through eqs 5 and 11 in the limit of large radii, which predict that the optical shift is insensitive to the QD size. These results extend the size range covered in earlier observations that did not report any size dependence of the pressure coefficient.[29] We call the regime where the mechanical response becomes size-dependent the extreme confinement (EC) regime. We now show the properties in the EC regime are unique by employing DFT calculations to understand the optical and mechanical properties under pressure in the EC regime.

DFT Structures. Although the structures of several magic sized CdSe clusters (MSCs) have been predicted,[60,61] most of them are based on stoichiometric bare clusters.[75−81] Day and co-workers have recently proposed an approach to deal with both tetrahedral CdSe MSCs[54] and CdS clusters using neural networks,[82] but there is still a need for an integrated approach and discussion about the electronic structure of colloidal QDs with various surface chemistries and sizes. Therefore, we have calculated the ground-state geometries of WZ and ZB CdSe QDs of different sizes. The optimized structures are presented

https://doi.org/10.1021/acs.jpcc.3c00998
J. Phys. Chem. C 2023, 127, 8657−8669

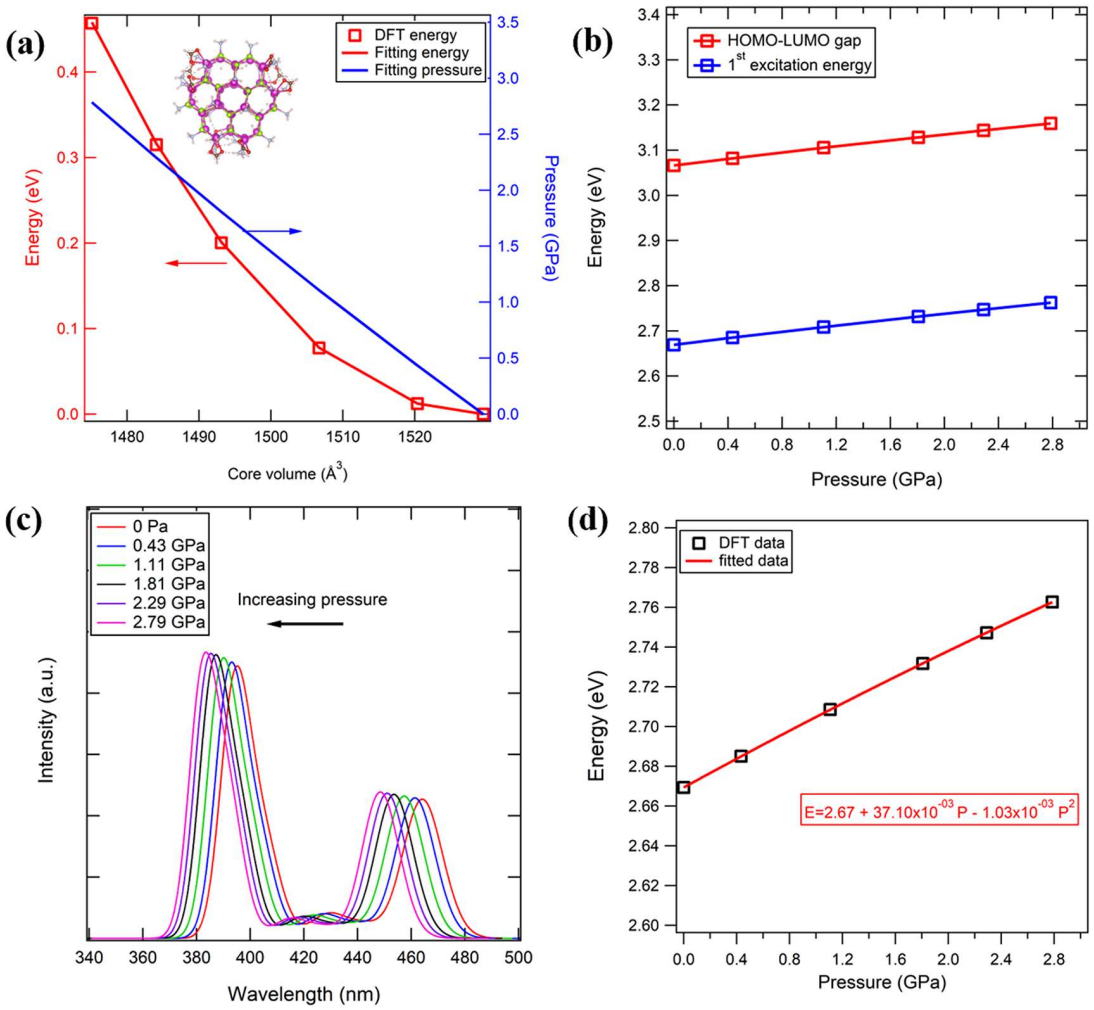

Figure 3. WZ-$(CdSe)_{45}$ QDs passivated by NH_3 and $HCOO^-$ QD, with H^+ as the counterion. (a) Energy and pressure fitting curves from eq 12. The energy at 0 GPa is set to 0 eV as the reference value. (b) Computed HOMO−LUMO gaps and first excitation energies under hydrostatic pressure. (c) Calculated absorption spectra under pressure showing the first three optical transitions. All three transitions undergo a blue-shift with increasing hydrostatic pressure. (d) Fit to the plot of first excitation energy vs pressure using eq 13.

in Figure 2. The geometries of all the optimized QDs deviate slightly from the initial WZ or ZB conformations; however, stable core structures are still recognizable.

Generally, the bonding of the commonly used carboxylate ligands to Cd atoms can be quite complicated and includes monodentate, bidentate, and bridging structures, as shown in ref 54. We use $HCOO^-$ to represent the binding of X-type ligands and NH_3 as a model for L-type ligand binding to Cd atoms. We denote the cadmium atoms in ZB and WZ structures using ZBnC and WZnC, respectively, where n is the coordination number with core Se atoms. With this notation the Cd atom at the apex of the ZB structures is characterized as ZB1C, and those at the edges are ZB2C while those within the facets are denoted as ZB3C. Similarly, the Cd atoms in WZ QDs are denoted as WZ2C and WZ3C for two- and three-coordinated Cd atoms, respectively.

Thus, while ZB1C atoms are typically coordinated to three ligands, ZB2C and WZ2C atoms tend to bind two ligands, while ZB3C atoms are attached to a single adsorbed ligand. In both WZ and ZB structures, the Cd atoms near the core center are coordinated to four Se atoms, and are denoted as WZ4C and ZB4C, respectively. Table S1 lists the average bond lengths of the optimized ZB and WZ QDs with full ligand passivation.

As shown in Figure 2a, the smallest ZB structure T_1 has a Cd_4Se core which needs six carboxylate ligands to balance the core positive charge, followed by six NH_3 ligands to saturate the rest of the Cd dangling bonds.

As a result, all facets are occupied by equal numbers of carboxylates and ammonia ligands. This also maximizes the number of hydrogen bonds. There is only one kind of Cd−Se bond in this cluster, i.e., Se−ZB1C, which has an average bond length of roughly 2.66 Å, and all of the Cd atoms are surface atoms. As the cluster grows, different Cd−Se bond types appear. For instance, Se−ZB2C type bonds appear in the T_2 structure, while three-coordinated Cd arises in the $Cd_{20}Se_{10}$ core. Above the $Cd_{35}Se_{20}$ cluster (T_4), a tetrahedral Cd-core configuration starts to be observed for the ZB structures. The bond lengths of Cd−Se pairs in the deep core area are slightly greater than those at the surfaces, edges, and vertices, suggesting that the ligand interaction modifies the surface chemistry of CdSe cores. Bond distances of 2.23−2.30 Å between N and Cd indicate that bond formation occurs for the neutral L-type group instead of Van der Waals interactions. The major binding mode for the formate ligand is through a

https://doi.org/10.1021/acs.jpcc.3c00998
J. Phys. Chem. C 2023, 127, 8657−8669

single oxygen atom, which binds to a surface Cd atom, enabling the other oxygen atom to form a hydrogen bond with a neighboring NH_3 group. However, two oxygens in the same formate group do occasionally bond in a bidentate fashion to the same Cd atom, slightly reducing the bond lengths. The coordination effects of X- and L-type ligands significantly enhance the stability of ZB-QDs, while maintaining the basic core tetrahedral structure.

To illustrate the importance of ligand passivation on electronic structures, all the surface NH_3 ligands are first removed. The surface undergoes reconstruction and the ligand binding behavior changes correspondingly, as shown in Figure S4a. Interestingly, the tetrahedral core structure is still observed but with a high degree of bond angle twisting. To compensate, two oxygen atoms on the majority of the formate groups bind to two different Cd atoms. The remaining formate groups behave as bidentate ligands, with two oxygen atoms bonding to the same Cd atom. Consequently, the number of dangling surface bonds is significantly reduced without altering core features. However, because of the electroneutrality rule, formate groups cannot be further removed.

In contrast, the WZ structures in our cases do not require the ligands to balance the total particle charge due to the intrinsically neutral stoichiometry of the core. To keep the wurtzite characteristics, a minimum of two, stacked, six-membered rings are required, making $(CdSe)_6$ the smallest WZ-CdSe QD. As a result, a near cubic structure with four nonequivalent six-membered ring faces is acquired. The $HCOO^-$ group forms two hydrogen bonds with H atoms from the NH_3 ligands of the same WZ2C and also the closest WZ3C NH_3.

The average Cd−Se bond length is 2.69 Å for facet Cd atoms and just 2.61 Å for the edge Cd atoms, which is a significant deviation from the QD core/bulk values. This indicates that there is significant bond relaxation in the presence of ligands, particularly near the surface or edge of the QD. Thus, the bond lengths of the low coordination number Cd−Se bonds appear to be shorter than those near the core for QDs of all sizes. The Cd−N bond lengths of three-coordinated Cd atoms are slightly longer than those in the two-coordinated structures, except for the smallest clusters which have the same length for different Cd environments. There are no significant differences for Cd−O bonds, which are roughly 2.30 Å. Compared to ZB QDs, WZ QDs are stabilized even without any ligand passivation due to their intrinsic tendency to form stoichiometric crystals. Figure S3b shows the ligand removal process for WZ-$(CdSe)_{15}$. After removing all of the surface ligands, the core structure relaxes significantly away from the WZ structure of the ligand-protected QD. The core structure reconstruction of the WZ structure is a consequence of the crystal minimizing the number of surface dangling bonds (also called self-healing[83]). Thus, surface reconstruction is likely to be more severe without multiligand or multidentate ligand passivation, especially for smaller QDs.

Pressure Dependence. To analyze the bulk modulus of QDs with different sizes in the EC regime, eq 13 was utilized to fit the energy in DFT calculations based on particle size. The bulk modulus was then obtained through this fitting, and pressure was calculated using eq 12 and the bulk modulus value. To compare with experiment, all WZ and ZB QDs were contracted uniformly without stretching, leaving the ligands free to relax.

As an example, computed DFT energies with respect to the core volume of a WZ-$(CdSe)_{45}$ cluster fitted from eq 13 are presented in Figure 3a. The BM equation yields a fairly good fit. When the core volume decreases, both the internal energy and pressure increase, as expected intuitively. The bulk modulus B_0 and its first pressure derivative B_0' are estimated to be 69.80 GPa and 4.82, respectively. Compared to the modulus of the bulk material (roughly 53 GPa from experiment,[84,85] and 44 GPa from the calculations on our largest clusters), these values are noticeably larger, indicating that small QDs are more rigid, which is consistent with the previously reported bulk modulus enhancement for small sizes,[38,86,87] and also consistent with the increase in phase transition pressure for NCs compared to the bulk.[88,89] A similar analysis for ZB-$Cd_{35}Se_{20}$ can be found in Figure S9, which yields B_0 = 81.51 GPa and B_0' = 4.00.

Time-dependent density functional theory calculations offer a computational approach for investigating pressure effects on the optical properties of CdSe QDs. The computed HOMO−LUMO gaps and first excitation energies for the compressed geometries are depicted in Figure 3b, and the TD-DFT electronic absorption spectra of WZ-$(CdSe)_{45}$ under hydrostatic pressure are shown in Figure 3c. Clearly, as the pressure increases, the absorption peak wavelength and the HOMO−LUMO gap both significantly blue-shift from their values under ambient pressure. Both the excitation energies and the HOMO−LUMO gap exhibit a near linear dependence on P which results in nearly unchanged exciton binding energies (estimated to be the difference between the HOMO−LUMO gap and the first excitation energy).

The computed absorption band gaps are fitted by second-order Taylor expansion by analogy with eq 2 as a function of pressure. The result is depicted in Figure 3d, giving α = 37.10 meV/GPa and $\beta = -1.03 \times 10^{-3}$ eV/GPa^2, which is in good agreement with the previous theoretical values of 39 meV/GPa[90] and close to the experimentally measured values of 43−58 meV/GPa[71−73] and our own experimental data in Figure 4.

The most important term is α, especially when the hydrostatic pressure is comparatively low and in the absence of phase transitions. According to "empirical rules" proposed by Paul,[91] α only depends on the interband transition type, and it determines the valence band and conduction band contributions to the band gap deformation. For bulk materials, Zunger and co-workers[92] showed that the energy of the conduction band minimum (CBM) Γ_{6c} state increases as the size decreases, while the influence on the valence band maximum (VBM) Γ_{8v} states is usually smaller and will generally increase with pressure for materials containing occupied d states but decrease for those without occupied d orbitals. As a result, the values of α for CdSe will always be positive due to the contributions of the d orbitals to the Cd atoms.

The calculated bulk modulus and optical shift α for WZ QDs as a function of size are given in Figure 4, and the related values are listed in Table 1. We note that the overestimation of bulk modulus absolute values by calculations may stem from the choice of functionals, but our calculation trend consistently matches our experimental results.[93] The experimentally determined value of the bulk modulus of the WZ structures decreases gradually as the size increases until it reaches a plateau value of 53 GPa, which is similar to values of the bulk material. The theoretically calculated bulk modulus of WZ-CdSe in the plateau region is 55 GPa, based on the Birch−

https://doi.org/10.1021/acs.jpcc.3c00998
J. Phys. Chem. C 2023, 127, 8657−8669

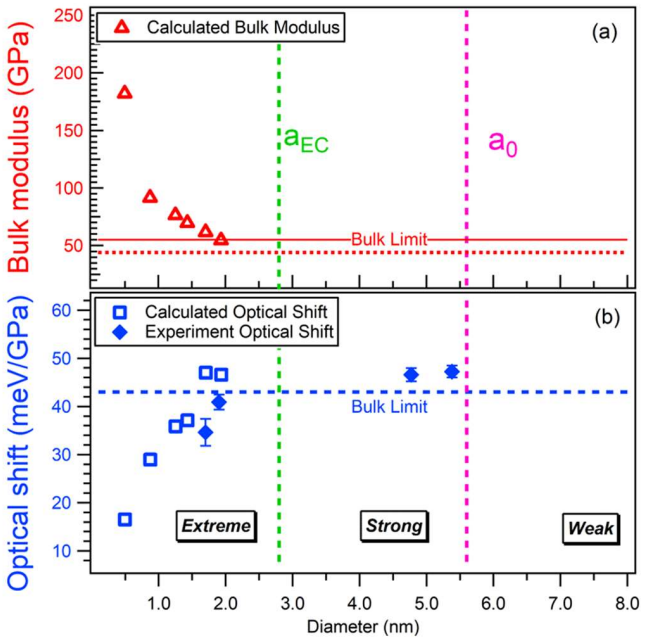

Figure 4. (a) Bulk modulus for WZ-CdSe as a function of the QD size. The horizontal lines show the bulk limit as determined experimentally (53 GPa, solid line)[84,85] and theoretically (44 GPa, dashed line). (b) Optical shift for WZ-CdSe as a function of the QD size based on our experimental absorption measurements. The bulk limit is assumed to be 43 meV/GPa.[71] The vertical lines indicate the three quantum confinement regimes, i.e., extreme, strong, and weak, which are demarcated by the extreme confined radius a_{EC} and Bohr radius a_0, respectively.

Table 1. Calculated Bulk Modulus and the Optical Absorption Shift of Different Sized ZB- and WZ-CdSe QDs and Experimental Bulk Values for Large WZ-CdSe QDs

ZB volume (Å^3)	ZB diameter (nm)	modulus (GPa)	optical shift (meV/GPa)
9.10	0.26	335.22	7.79
94.15	0.56	133.56	21.93
312.00	0.84	98.83	30.04
777.06	1.14	81.51	36.64
1436.46	1.40	76.83	36.75
3733.42	1.93	51.16	46.76
∞	∞	45.00[a,b]	
WZ volume (Å^3)	WZ diameter (nm)	modulus (GPa)	optical shift (meV/GPa)
63.83	0.50	182.13	16.53
350.92	0.88	91.69	28.96
1026.51	1.25	76.47	35.90
1529.51	1.43	69.80	37.10
2584.73	1.70	61.69	47.00
5195.46	1.93	54.69	46.61
∞	∞	44.00[a,b]	
experimental values[c]			
2571.14	1.70		34.70
4186.67	2.00		41.00
56086.61	4.75		46.50
87069.58	5.50		47.20

[a]Calculated in this work. [b]Bulk modulus values from ref 94. [c]Experimental optical shift in this work.

Murnaghan equation fitting, which is close to both the experimental value and other theoretically determined WZ-CdSe values (44 GPa).

Surprisingly, the size regime where the pressure response becomes size dependent is approximately 2 times smaller than the Bohr radius a_0 of CdSe (~5.6 nm). The higher values for the bulk modulus are consistent with earlier values obtained with pesudo-hydrogen passivated CdSe QDs,[38] and for extremely small NC sizes the bulk modulus is 6 times larger than for the bulk crystal. The deviation in the bulk modulus for the ZB structure has been proposed by Cohen to follow a scaling law obeying $R^{-3.5}$ with respect to the particle radius by only taking the nearest-neighbor distances into consideration, which means the approximation that α is a constant is reasonable even in the moderate size regime as given in eq 9.

For the optical shifts α, similar behavior is observed with strong shifts in the EC regime but the shifts quickly plateau out at values of 47 meV/GPa in the strong regime (note that the reference values range from 37 to 58 meV[71,72]). Hence, the optical shifts of both WZ and ZB structures exhibit a size dependence only within the EC regime. When the particle radius exceeds a_{EC}, α is independent of QD size.

Electronic Structure–Properties. Electronic structure analysis can be used to further understand the intrinsic origins underpinning the size-dependent optical shifts and bulk modulus of CdSe QDs within the EC regime. The projected density of states (PDOS) is a very valuable tool for visual study of orbital composition. The PDOS of fragment A is defined as

$$\mathrm{PDOS_A}(E) = \sum_i \Theta_{i,\mathrm{A}} \delta(E - \varepsilon_i) \tag{14}$$

where $\Theta_{i,A}$ is the composition of fragment A in orbital i, and δ stands for the Dirac delta function. The total density of states (DOS) is the summation of all the fragment contributions. DOS and PDOS can be visualized using a Gaussian profile

$$A(\omega) = \frac{1}{\sigma\sqrt{\pi}} \sum_n c_n \exp \frac{-(\omega_n - \omega)^2}{\sigma^2} \tag{15}$$

where ω_n is the energy, c_n is the intensity of the transition, and σ is the width of a given peak. DOS and PDOS spectra are simulated using σ = 200 meV in all of our cases.

Figure S5 shows the calculated PDOS for six typical structures, ranging from small (WZ-$(CdSe)_{15}$, ZB-$Cd_{10}Se_4$) and medium-sized clusters (WZ-$(CdSe)_{45}$, ZB-$Cd_{35}Se_{20}$), up to relatively large clusters (WZ-$(CdSe)_{122}$, ZB-$Cd_{120}Se_{84}$) at 0 GPa. For small WZ QDs, Se p-orbital features are observed at the valence band (VB) edge, whereas Cd orbitals dominate the conduction band (CB) edge. In comparison, for small size ZB-QDs, the VB edge is largely contributed to by the overlap of Se orbitals and the O orbitals from the carboxylate ligands, while the CB edge is still dominated by Cd orbitals. Because of our passivation approach, no defect states are observed between the CBM and VBM. For WZ-$(CdSe)_{15}$, WZ-$(CdSe)_{45}$, ZB-$Cd_{10}Se_4$, and ZB-$Cd_{35}Se_{20}$, there are considerable DOS contributions from the ligands, highlighting the fact that the ligand–core coupling is non-negligible for smaller sized QDs. In addition to the pressure-induced interband crossing, the results of our modeling also indicate the surface ligand states are likely to couple to electronic levels in the CdSe core. As the size of the QDs increases, the contribution from Cd orbitals starts to become important around the VB edge and also the Se contributions near the CBM. As a result, both Cd and Se

https://doi.org/10.1021/acs.jpcc.3c00998
J. Phys. Chem. C 2023, 127, 8657−8669

orbital character can be discerned at the band edge of large QDs. At the same time, the ligands contribute less to the band edge states as the QD size increases, indicating the diminishing impact of ligands on the optical properties for larger QDs, which is one of the major differences between small QDs and large QDs. However, even when QDs are in the intermediate size regime (e.g., WZ-$(CdSe_{122})$ and ZB-$Cd_{120}Se_{84}$), bulk-like DOS is observed near the band edge. When increasing the pressure from 0 to 4 GPa, only mild CBM blue-shifts are found, and the DOS features are maintained for intermediate-sized QDs (Figure 5). Conversely, there are relatively large differences in the DOS for smaller QDs before and after imposition of hydrostatic pressures.

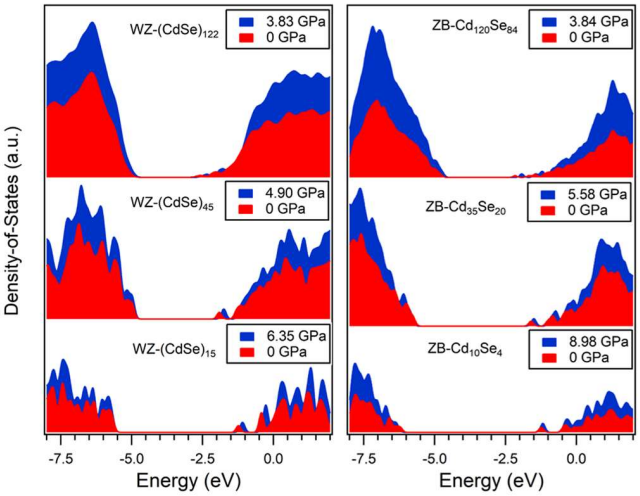

Figure 5. Total density of states of CdSe with different sizes at different applied hydrostatic pressures. Left panels: wurtzite structures $(CdSe)_y$, y = 15, 45, and 122. Right panels: zinc-blende structures T_x, x = 2, 4, and 8. Structures under pressure were calculated at 2% compression with respect to the ground-state geometries, assuming phase transformations do not occur.

Figures S7 and S8 show the resulting molecular orbitals (MOs) for the three lowest occupied orbitals (HOMO, HOMO−1, HOMO−2) and three unoccupied orbitals (LUMO, LUMO+1, LUMO+2) for three WZ $(CdSe)_{15}$, $(CdSe)_{45}$, and $(CdSe)_{122}$ and ZB structures $Cd_{15}Se_4$, $Cd_{35}Se_{20}$, and $Cd_{120}Se_{84}$ at 0 GPa, respectively. For smaller QD sizes, the HOMOs possess almost even spatial distributions delocalized over the CdSe core, but with higher weight on the Se atoms for both WZ and ZB QDs. Additionally, oxygen contributions from the carboxylate ligands to the HOMO in ZB QDs are found to be more extensive than for WZ QDs, indicating greater ligand−core interactions in ZB QDs, even though no conjugated ligands are used. Similarly, the LUMO is delocalized over the entire core and over a fraction of the surface ligands for small QDs. Such frontier MO delocalization was also found in previously reported small CdS clusters.[27] In contrast, as the QD size increases, the frontier orbitals become more localized. Both HOMO and LUMO orbitals localize near the QD corners instead of being spread over the whole particle core, which is in agreement with previously reported size-dependent $CsPbBr_3$ perovskite systems.[95] Hence, when exerting external pressure, the delocalized HOMO and LUMO orbitals will be more evenly distributed over the semiconductor core.

Finally, we note that in the EC regime the differences between the pressure coefficients α for absorption and PL are negative and increase in magnitude with decreasing QD size. However, above the EC regime, this difference is positive and becomes size independent. The pressure-induced Stokes shift has been observed for TOPO and TBPO capped 3.3 nm CdSe QDs previously when the nanocrystals are in the form of dilute solutions or solid films.[96] It was found the surface states have only a small influence on the pressure-induced Stokes shift,[96] which is consistent with what we observed above the EC regime.

CONCLUSION

In summary, by combining diamond anvil experiments and DFT calculations, we find that the bulk modulus of small CdSe nanocrystals does not begin to diverge from bulk behavior until well below the usual weak and strong quantum size regimes. We denote this third size regime the "extreme confinement" (EC) regime. Conversely, it seems mechanical properties of nanocrystals approach bulk behavior at surprisingly small particle sizes. In the EC regime, frontier molecular orbitals are delocalized over the whole QD, and the surface chemistry plays an extremely important role. In the EC regime, the effective mass and dielectric constant are expected to be pressure dependent, leading to a breakdown of the Brus equation. Although we have only investigated the pressure dependence of semiconductor nanocrystals in the EC regime, we expect other novel phenomena to occur within this regime.

ASSOCIATED CONTENT

Supporting Information

The Supporting Information is available free of charge at https://pubs.acs.org/doi/10.1021/acs.jpcc.3c00998.

Chosen functionals, calculated structures, density of states, absorption spectra and molecular orbitals resulting from the DFT calculations, and details of the experimental absorption and PL spectra (PDF)

AUTHOR INFORMATION

Corresponding Author

Paul Mulvaney − *ARC Centre of Excellence in Exciton Science, School of Chemistry, The University of Melbourne, Parkville, VIC 3010, Australia;* orcid.org/0000-0002-8007-3247; Email: mulvaney@unimelb.edu.au

Authors

Zifei Chen − *ARC Centre of Excellence in Exciton Science, School of Chemistry, The University of Melbourne, Parkville, VIC 3010, Australia;* orcid.org/0000-0003-4341-496X

J. Curtis Beimborn, II − *JILA and the Department of Chemistry, University of Colorado, Boulder, Colorado 80309-0440, United States*

Nicholas Kirkwood − *ARC Centre of Excellence in Exciton Science, School of Chemistry, The University of Melbourne, Parkville, VIC 3010, Australia;* orcid.org/0000-0002-7845-7081

Salvy P. Russo − *ARC Centre of Excellence in Exciton Science, School of Science, RMIT University, Melbourne 3000, Australia;* orcid.org/0000-0003-3589-3040

J. Mathias Weber − *JILA and the Department of Chemistry, University of Colorado, Boulder, Colorado 80309-0440, United States;* orcid.org/0000-0002-5493-5886

https://doi.org/10.1021/acs.jpcc.3c00998
J. Phys. Chem. C 2023, 127, 8657−8669

Complete contact information is available at:
https://pubs.acs.org/10.1021/acs.jpcc.3c00998

Notes

The authors declare no competing financial interest.

■ ACKNOWLEDGMENTS

Z.C., N.K., S.R., and P.M. thank the ARC for support through CE170100026. Z.C. thanks the Australian Government and the University of Melbourne for a Research Training Program (RTP) Scholarship. The computational work was performed using computational resources provided by the Australian Government through the National Computational Infrastructure (NCI) Facility and the Pawsey Supercomputer Centre. Electron microscopy was performed at the Ian Holmes Imaging Centre. C.B. and J.M.W. gratefully acknowledge the National Science Foundation for support through the JILA AMO Physics Frontier Center under Grant PHY-1734006. Acknowledgment is also made to the Donors of the American Chemical Society Petroleum Research Fund for partial support of this research.

■ REFERENCES

(1) Wang, Z.; Mohamed, M.; Link, S.; El-Sayed, M. Crystallographic facets and shapes of gold nanorods of different aspect ratios. *Surf. Sci.* **1999**, *440*, L809−L814.
(2) Koch, C. C. Structural nanocrystalline materials: an overview. *J. Mater. Sci.* **2007**, *42*, 1403−1414.
(3) Hu, M.; Hillyard, P.; Hartland, G. V.; Kosel, T.; Perez-Juste, J.; Mulvaney, P. Determination of the Elastic Constants of Gold Nanorods Produced by Seed Mediated Growth. *Nano Lett.* **2004**, *4*, 2493−2497.
(4) Cheng, H.-W.; Chang, Y.-C.; Tang, S.-N.; Yuan, C.-T.; Tang, J.; Tseng, F.-G. Characterization of single 1.8-nm Au nanoparticle attachments on AFM tips for single sub-4-nm object pickup. *Nanoscale Res. Lett.* **2013**, *8*, 482.
(5) Ducker, W. A.; Senden, T. J.; Pashley, R. M. Direct measurement of colloidal forces using an atomic force microscope. *Nature* **1991**, *353*, 239−241.
(6) Mak, L. H.; Knoll, M.; Weiner, D.; Gorschlüter, A.; Schirmeisen, A.; Fuchs, H. Reproducible attachment of micrometer sized particles to atomic force microscopy cantilevers. *Rev. Sci. Instrum.* **2006**, *77*, 046104.
(7) Lantz, M. A.; Jarvis, S. P.; Tokumoto, H. High resolution eddy current microscopy. *Appl. Phys. Lett.* **2001**, *78*, 383−385.
(8) Clark, S. C.; Walz, J. Y.; Ducker, W. A. Atomic Force Microscopy Colloid-Probe Measurements with Explicit Measurement of Particle-Solid Separation. *Langmuir* **2004**, *20*, 7616−7622.
(9) Ong, Q. K.; Sokolov, I. Attachment of nanoparticles to the AFM tips for direct measurements of interaction between a single nanoparticle and surfaces. *J. Colloid Interface Sci.* **2007**, *310*, 385−390.
(10) Vakarelski, I. U.; Brown, S. C.; Moudgil, B. M.; Higashitani, K. Nanoparticle-terminated scanning probe microscopy tips and surface samples. *Adv. Powder Technol.* **2007**, *18*, 605−614.
(11) Vakarelski, I. U.; Higashitani, K. Single-Nanoparticle-Terminated Tips for Scanning Probe Microscopy. *Langmuir* **2006**, *22*, 2931−2934.
(12) Wang, H.; Tian, T.; Zhang, Y.; Pan, Z.; Wang, Y.; Xiao, Z. Sequential Electrochemical Oxidation and Site-Selective Growth of Nanoparticles onto AFM Probes. *Langmuir* **2008**, *24*, 8918−8922.
(13) Mie, G. Beiträge zur Optik trüber Medien, speziell kolloidaler Metallösungen. *Ann. Phys. (Leipzig)* **1908**, *330*, 377−445.
(14) Martín-Sánchez, C.; Barreda-Argüeso, J. A.; Seibt, S.; Mulvaney, P.; Rodríguez, F. Effects of Hydrostatic Pressure on the Surface Plasmon Resonance of Gold Nanocrystals. *ACS Nano* **2019**, *13*, 498−504.
(15) Martín-Sánchez, C.; González-Rubio, G.; Mulvaney, P.; Guerrero-Martínez, A.; Liz-Marzán, L. M.; Rodríguez, F. Monodisperse Gold Nanorods for High-Pressure Refractive Index Sensing. *J. Phys. Chem. Lett.* **2019**, *10*, 1587−1593.
(16) Balchan, A. S.; Drickamer, H. G. High Pressure High Temperature Optical Device. *Rev. Sci. Instrum.* **1960**, *31*, 511−513.
(17) Tolbert, S. H.; Alivisatos, A. P. Size dependence of the solid-solid phase transition in CdSe nanocrystals. *Z. Phys. D Atom Mol. Cl.* **1993**, *26*, 56−58.
(18) Wang, L.; Yang, W.; Ding, Y.; Ren, Y.; Xiao, S.; Liu, B.; Sinogeikin, S. V.; Meng, Y.; Gosztola, D. J.; Shen, G.; Hemley, R. J.; Mao, W. L.; Mao, H.-k. Size-Dependent Amorphization of Nanoscale Y_2O_3 at High Pressure. *Phys. Rev. Lett.* **2010**, *105*, 095701.
(19) Quan, Z.; Wang, Y.; Bae, I.-T.; Loc, W. S.; Wang, C.; Wang, Z.; Fang, J. Reversal of Hall−Petch Effect in Structural Stability of PbTe Nanocrystals and Associated Variation of Phase Transformation. *Nano Lett.* **2011**, *11*, 5531−5536.
(20) Swamy, V.; Kuznetsov, A.; Dubrovinsky, L. S.; McMillan, P. F.; Prakapenka, V. B.; Shen, G.; Muddle, B. C. Size-Dependent Pressure-Induced Amorphization in Nanoscale TiO_2. *Phys. Rev. Lett.* **2006**, *96*, 135702.
(21) Yuan, H.; Wang, K.; Li, S.; Tan, X.; Li, Q.; Yan, T.; Cheng, B.; Yang, K.; Liu, B.; Zou, G.; Zou, B. Direct Zircon-to-Scheelite Structural Transformation in YPO4 and YPO4:Eu3+ Nanoparticles Under High Pressure. *J. Phys. Chem. C* **2012**, *116*, 24837−24844.
(22) Wu, H.; Bai, F.; Sun, Z.; Haddad, R. E.; Boye, D. M.; Wang, Z.; Huang, J. Y.; Fan, H. Nanostructured Gold Architectures Formed through High Pressure-Driven Sintering of Spherical Nanoparticle Arrays. *J. Am. Chem. Soc.* **2010**, *132*, 12826−12828.
(23) Wang, Z.; Schliehe, C.; Wang, T.; Nagaoka, Y.; Cao, Y. C.; Bassett, W. A.; Wu, H.; Fan, H.; Weller, H. Deviatoric Stress Driven Formation of Large Single-Crystal PbS Nanosheet from Nanoparticles and in Situ Monitoring of Oriented Attachment. *J. Am. Chem. Soc.* **2011**, *133*, 14484−14487.
(24) Yang, X.; Wang, Y.; Wang, K.; Sui, Y.; Zhang, M.; Li, B.; Ma, Y.; Liu, B.; Zou, G.; Zou, B. Polymorphism and Formation Mechanism of Nanobipods in Manganese Sulfide Nanocrystals Induced by Temperature or Pressure. *J. Phys. Chem. C* **2012**, *116*, 3292−3297.
(25) Xiao, N.; Zhu, L.; Wang, K.; Dai, Q.; Wang, Y.; Li, S.; Sui, Y.; Ma, Y.; Liu, J.; Liu, B.; Zou, G.; Zou, B. Synthesis and high-pressure transformation of metastable wurtzite-structured CuGaS2 nanocrystals. *Nanoscale* **2012**, *4*, 7443−7447.
(26) Koh, W.-k.; Dandu, N. K.; Fidler, A. F.; Klimov, V. I.; Pietryga, J. M.; Kilina, S. V. Thickness-Controlled Quasi-Two-Dimensional Colloidal PbSe Nanoplatelets. *J. Am. Chem. Soc.* **2017**, *139*, 2152−2155.
(27) Corsini, N. R. C.; Hine, N. D. M.; Haynes, P. D.; Molteni, C. Unravelling the Roles of Size, Ligands, and Pressure in the Piezochromic Properties of CdS Nanocrystals. *Nano Lett.* **2017**, *17*, 1042−1048.
(28) Meulenberg, R. W.; Jennings, T.; Strouse, G. F. Compressive and tensile stress in colloidal CdSe semiconductor quantum dots. *Phys. Rev. B* **2004**, *70*, 235311.
(29) Meulenberg, R. W.; Strouse, G. F. Pressure-induced electronic coupling in CdSe semiconductor quantum dots. *Phys. Rev. B* **2002**, *66*, 035317.
(30) Xiao, G.; Wang, Y.; Han, D.; Li, K.; Feng, X.; Lv, P.; Wang, K.; Liu, L.; Redfern, S. A. T.; Zou, B. Pressure-Induced Large Emission Enhancements of Cadmium Selenide Nanocrystals. *J. Am. Chem. Soc.* **2018**, *140*, 13970−13975.
(31) Liu, J.; Kilina, S. V.; Tretiak, S.; Prezhdo, O. V. Ligands Slow Down Pure-Dephasing in Semiconductor Quantum Dots. *ACS Nano* **2015**, *9*, 9106−9116.
(32) Kilina, S.; Kilin, D.; Tretiak, S. Light-Driven and Phonon-Assisted Dynamics in Organic and Semiconductor Nanostructures. *Chem. Rev.* **2015**, *115*, 5929−5978.
(33) Beimborn, J. C.; Walther, L. R.; Wilson, K. D.; Weber, J. M. Size-Dependent Pressure-Response of the Photoluminescence of CsPbBr3 Nanocrystals. *J. Phys. Chem. Lett.* **2020**, *11*, 1975−1980.

(34) Liu, X.; Xu, K.; Ni, Y.; Lu, P.; Wang, G.; He, L. Strain-dependent elastic asymmetry of alkylthiol-coated gold superlattices: An atomistic molecular dynamics study. *J. Appl. Phys.* **2022**, *132*, 075104.
(35) Makeev, M. A.; Madhukar, A. Simulations of Atomic Level Stresses in Systems of Buried Ge /Si Islands. *Phys. Rev. Lett.* **2001**, *86*, 5542−5545.
(36) Zanjani, M. B.; Lukes, J. R. Size dependent elastic moduli of CdSe nanocrystal superlattices predicted from atomistic and coarse grained models. *J. Chem. Phys.* **2013**, *139*, 144702.
(37) Kelley, A. M. Comparison of three empirical force fields for phonon calculations in CdSe quantum dots. *J. Chem. Phys.* **2016**, *144*, 214702.
(38) Cherian, R.; Gerard, C.; Mahadevan, P.; Cuong, N. T.; Maezono, R. Size dependence of the bulk modulus of semiconductor nanocrystals from first-principles calculations. *Phys. Rev. B* **2010**, *82*, 235321.
(39) Kamisaka, H.; Kilina, S. V.; Yamashita, K.; Prezhdo, O. V. Ab Initio Study of Temperature and Pressure Dependence of Energy and Phonon-Induced Dephasing of Electronic Excitations in CdSe and PbSe Quantum Dots. *J. Phys. Chem. C* **2008**, *112*, 7800−7808.
(40) Rabani, E.; Hetényi, B.; Berne, B. J.; Brus, L. E. Electronic properties of CdSe nanocrystals in the absence and presence of a dielectric medium. *J. Chem. Phys.* **1999**, *110*, 5355−5369.
(41) Huang, X.; Lindgren, E.; Chelikowsky, J. R. Surface passivation method for semiconductor nanostructures. *Phys. Rev. B* **2005**, *71*, 165328.
(42) Brus, L. Electronic wave functions in semiconductor clusters: experiment and theory. *J. Phys. Chem.* **1986**, *90*, 2555−2560.
(43) Brus, L. E. Electron−electron and electron-hole interactions in small semiconductor crystallites: The size dependence of the lowest excited electronic state. *J. Chem. Phys.* **1984**, *80*, 4403−4409.
(44) Kayanuma, Y. Quantum-size effects of interacting electrons and holes in semiconductor microcrystals with spherical shape. *Phys. Rev. B* **1988**, *38*, 9797−9805.
(45) Cohen, M. L. Calculation of bulk moduli of diamond and zinc-blende solids. *Phys. Rev. B* **1985**, *32*, 7988−7991.
(46) Murnaghan, F. D. Finite Deformations of an Elastic Solid. *Am. J. Math.* **1937**, *59*, 235−260.
(47) Birch, F. Finite Elastic Strain of Cubic Crystals. *Phys. Rev.* **1947**, *71*, 809−824.
(48) Van Embden, J.; Mulvaney, P. Nucleation and Growth of CdSe Nanocrystals in a Binary Ligand System. *Langmuir* **2005**, *21*, 10226−10233.
(49) Peng, Z. A.; Peng, X. Formation of High-Quality CdTe, CdSe, and CdS Nanocrystals Using CdO as Precursor. *J. Am. Chem. Soc.* **2001**, *123*, 183−184.
(50) Čapek, R. K.; Lambert, K.; Dorfs, D.; Smet, P. F.; Poelman, D.; Eychmüller, A.; Hens, Z. Synthesis of Extremely Small CdSe and Bright Blue Luminescent CdSe/ZnS Nanoparticles by a Prefocused Hot-Injection Approach. *Chem. Mater.* **2009**, *21*, 1743−1749.
(51) Beimborn, J. C.; Hall, L. M. G.; Tongying, P.; Dukovic, G.; Weber, J. M. Pressure Response of Photoluminescence in Cesium Lead Iodide Perovskite Nanocrystals. *J. Phys. Chem. C* **2018**, *122*, 11024−11030.
(52) Holzapfel, W. B. Refinement of the ruby luminescence pressure scale. *J. Appl. Phys.* **2003**, *93*, 1813−1818.
(53) Grant, C. D.; Crowhurst, J. C.; Hamel, S.; Williamson, A. J.; Zaitseva, N. Anomalous Photoluminescence in CdSe Quantum-Dot Solids at High Pressure Due to Nonuniform Stress. *Small* **2008**, *4*, 788−794.
(54) Nguyen, K. A.; Pachter, R.; Jiang, J.; Day, P. N. Systematic Study of Structure, Stability, and Electronic Absorption of Tetrahedral CdSe Clusters with Carboxylate and Amine Ligands. *J. Phys. Chem. A* **2018**, *122*, 6704−6712.
(55) Beecher, A. N.; Yang, X.; Palmer, J. H.; LaGrassa, A. L.; Juhas, P.; Billinge, S. J. L.; Owen, J. S. Atomic Structures and Gram Scale Synthesis of Three Tetrahedral Quantum Dots. *J. Am. Chem. Soc.* **2014**, *136*, 10645−10653.
(56) Errandonea, D.; Gracia, L.; Lacomba-Perales, R.; Polian, A.; Chervin, J. C. Compression of scheelite-type SrMoO4 under quasi-hydrostatic conditions: Redefining the high-pressure structural sequence. *J. Appl. Phys.* **2013**, *113*, 123510.
(57) Ruiz-Fuertes, J.; Friedrich, A.; Errandonea, D.; Segura, A.; Morgenroth, W.; Rodríguez-Hernández, P.; Muñoz, A.; Meng, Y. Optical and structural study of the pressure-induced phase transition of $CdWO_4$. *Phys. Rev. B* **2017**, *95*, 174105.
(58) Adamo, C.; Barone, V. Toward Reliable Density Functional Methods without Adjustable Parameters: The PEB0Model. *J. Chem. Phys.* **1999**, *110*, 6158−6170.
(59) *TURBOMOLE V7.2 2017, a development of University of Karlsruhe and Forschungszentrum Karlsruhe GmbH*, 1989−2007, TURBOMOLE GmbH, since 2007; available from http://www.turbomole.com.
(60) Nguyen, K.; Pachter, R.; Day, P. N. Computational Prediction of Structures and Optical Excitations for Nanoscale Ultrasmall ZnS and CdSe Clusters. *J. Chem. Theory. Comput.* **2013**, *9*, 3581−3596.
(61) Nguyen, K.; Pachter, R.; Day, P. N.; Su, H. Theoretical Analysis of Structures and Electronic Spectra in Molecular Cadmium Chalcogenide Clusters. *J. Chem. Phys.* **2015**, *142*, 234305.
(62) Krack, M.; Parrinello, M. Quickstep: Make the atoms dance; *High Performance Computing in Chemistry*, 2004; pp 29−51.
(63) VandeVondele, J.; Krack, M.; Mohamed, F.; Parrinello, M.; Chassaing, T.; Hutter, J. Quickstep: Fast and accurate density functional calculations using a mixed Gaussian and plane waves approach. *Comput. Phys. Commun.* **2005**, *167*, 103−128.
(64) Ding, Y.; Hassanali, A. A.; Parrinello, M. Anomalous water diffusion in salt solutions. *Proc. Natl. Acad. Sci. U. S. A.* **2014**, *111*, 3310−3315.
(65) Perdew, J. P.; Burke, K.; Ernzerhof, M. Generalized Gradient Approximation Made Simple. *Phys. Rev. Lett.* **1996**, *77*, 3865−3868.
(66) Goedecker, S.; Teter, M.; Hutter, J. Separable dual-space Gaussian pseudopotentials. *Phys. Rev. B* **1996**, *54*, 1703−1710.
(67) VandeVondele, J.; Hutter, J. Gaussian basis sets for accurate calculations on molecular systems in gas and condensed phases. *J. Chem. Phys.* **2007**, *127*, 114105.
(68) Guidon, M.; Hutter, J.; VandeVondele, J. Robust Periodic Hartree-Fock Exchange for Large-Scale Simulations Using Gaussian Basis Sets. *J. Chem. Theory Comput.* **2009**, *5*, 3010−3021.
(69) Barber, C. B.; Dobkin, D. P.; Huhdanpaa, H. The Quickhull Algorithm for Convex Hulls. *ACM Trans. Math. Softw.* **1996**, *22*, 469−483.
(70) Lu, T.; Chen, F. Multiwfn: A multifunctional wavefunction analyzer. *J. Comput. Chem.* **2012**, *33*, 580−592.
(71) Shan, W.; Walukiewicz, W.; Ager, J. W.; Yu, K. M.; Wu, J.; Haller, E. E. Pressure dependence of the fundamental band-gap energy of CdSe. *Appl. Phys. Lett.* **2004**, *84*, 67−69.
(72) Edwards, A. L.; Drickamer, H. G. Effect of Pressure on the Absorption Edges of Some III-V, II-VI, and I-VII Compounds. *Phys. Rev.* **1961**, *122*, 1149−1157.
(73) Li, B.; Liu, W.; Zhu, X.; Lin, S.; Yang, Y.; Yang, Q.; Jin, P. Pressure-dependent photoluminescence of CdSe/ZnS quantum dots: Critical point of different pressure regimes. *Phys. Lett. A* **2019**, *383*, 1483−1486.
(74) Mei, J.; Lemos, V. Photoluminescence on CdSe and CdTe under hydrostatic pressure. *Solid State Commun.* **1984**, *52*, 785−788.
(75) Dmitruk, I.; Belosludov, R. V.; Dmytruk, A.; Noda, Y.; Barnakov, Y.; Park, Y.-S.; Kasuya, A. Experimental and Computational Studies of the Structure of CdSe Magic-Size Clusters. *J. Phys. Chem. A* **2020**, *124*, 3398−3406.
(76) Xie, Y.; Du, N.; Yu, S.; Zhang, L.; Yang, M. Unraveling the Structure-Dependent Radiative and Nonradiative Decays in (CdSe)13 Clusters through First-Principles Calculations. *J. Phys. Chem. C* **2019**, *123*, 30714−30722.
(77) Tan, L.; Pickard, C. J.; Yu, K.; Sapelkin, A.; Misquitta, A. J.; Dove, M. T. Structures of CdSe and CdS Nanoclusters from Ab Initio Random Structure Searching. *J. Phys. Chem. C* **2019**, *123*, 29370−29378.

https://doi.org/10.1021/acs.jpcc.3c00998
J. Phys. Chem. C 2023, 127, 8657−8669

(78) Hsieh, T.-E.; Yang, T.-W.; Hsieh, C.-Y.; Huang, S.-J.; Yeh, Y.-Q.; Chen, C.-H.; Li, E. Y.; Liu, Y.-H. Unraveling the Structure of Magic-Size (CdSe)13 Cluster Pairs. *Chem. Mater.* **2018**, *30*, 5468−5477.
(79) Gutsev, L. G.; Ramachandran, B. R.; Gutsev, G. L. Pathways of Growth of CdSe Nanocrystals from Nucleant (CdSe)34 Clusters. *J. Phys. Chem. C* **2018**, *122*, 3168−3175.
(80) Kuznetsov, A. E.; Beratan, D. N. Structural and Electronic Properties of Bare and Capped Cd33Se33 and Cd33Te33 Quantum Dots. *J. Phys. Chem. C* **2014**, *118*, 7094−7109.
(81) Del Ben, M.; Havenith, R. W. A.; Broer, R.; Stener, M. Density Functional Study on the Morphology and Photoabsorption of CdSe Nanoclusters. *J. Phys. Chem. C* **2011**, *115*, 16782−16796.
(82) Nguyen, K. A.; Pachter, R.; Day, P. N. Systematic Study of the Properties of CdS Clusters with Carboxylate Ligands Using a Deep Neural Network Potential Developed with Data from Density Functional Theory Calculations. *J. Phys. Chem. A* **2020**, *124*, 10472−10481.
(83) Puzder, A.; Williamson, A. J.; Gygi, F. m. c.; Galli, G. Self-Healing of CdSe Nanocrystals: First-Principles Calculations. *Phys. Rev. Lett.* **2004**, *92*, 217401.
(84) Sowa, H. The high-pressure behaviour of CdSe up to 3 GPa and the orientation relations between its wurtzite- and NaCl-type modifications. *Solid State Sci.* **2005**, *7*, 1384−1389.
(85) Wei, S.-H.; Zunger, A. Predicted band-gap pressure coefficients of all diamond and zinc-blende semiconductors: Chemical trends. *Phys. Rev. B* **1999**, *60*, 5404−5411.
(86) Gu, Q. F.; Krauss, G.; Steurer, W.; Gramm, F.; Cervellino, A. Unexpected High Stiffness of Ag and Au Nanoparticles. *Phys. Rev. Lett.* **2008**, *100*, 045502.
(87) Martín-Sánchez, C.; Sánchez-Iglesias, A.; Barreda-Argüeso, J. A.; Polian, A.; Itié, J.-P.; Pérez, J.; Mulvaney, P.; Liz-Marzán, L. M.; Rodríguez, F. On the Stiffness of Gold at the Nanoscale. *ACS Nano* **2021**, *15*, 19128−19137.
(88) Tolbert, S. H.; Alivisatos, A. P. High-Pressure Structural Transformations in Semiconductor Nanocrystals. *Annu. Rev. Phys. Chem.* **1995**, *46*, 595−626.
(89) Meng, L.; Lane, J. M. D.; Baca, L.; Tafoya, J.; Ao, T.; Stoltzfus, B.; Knudson, M.; Morgan, D.; Austin, K.; Park, C.; Chow, P.; Xiao, Y.; Li, R.; Qin, Y.; Fan, H. Shape Dependence of Pressure-Induced Phase Transition in CdS Semiconductor Nanocrystals. *J. Am. Chem. Soc.* **2020**, *142*, 6505−6510.
(90) Zhuravlev, K. K.; Pietryga, J. M.; Sander, R. K.; Schaller, R. D. Optical properties of PbSe nanocrystal quantum dots under pressure. *Appl. Phys. Lett.* **2007**, *90*, 043110.
(91) Camphausen, D. L.; Connell, G. A. N.; Paul, W. Calculation of Energy-Band Pressure Coefficients from the Dielectric Theory of the Chemical Bond. *Phys. Rev. Lett.* **1971**, *26*, 184−188.
(92) Fu, H.; Wang, L.-W.; Zunger, A. Excitonic exchange splitting in bulk semiconductors. *Phys. Rev. B* **1999**, *59*, 5568−5574.
(93) Zhang, G.-X.; Reilly, A. M.; Tkatchenko, A.; Scheffler, M. Performance of various density-functional approximations for cohesive properties of 64 bulk solids. *New J. Phys.* **2018**, *20*, 063020.
(94) de Jong, M.; Chen, W.; Geerlings, H.; Asta, M.; Persson, K. A. A database to enable discovery and design of piezoelectric materials. *Sci. Data* **2015**, *2*, 150053.
(95) Brennan, M. C.; Herr, J. E.; Nguyen-Beck, T. S.; Zinna, J.; Draguta, S.; Rouvimov, S.; Parkhill, J.; Kuno, M. Origin of the Size-Dependent Stokes Shift in CsPbBr3 Perovskite Nanocrystals. *J. Am. Chem. Soc.* **2017**, *139*, 12201−12208.
(96) Kim, B. S.; Islam, M. A.; Brus, L. E.; Herman, I. P. Interdot interactions and band gap changes in CdSe nanocrystal arrays at elevated pressure. *J. Appl. Phys.* **2001**, *89*, 8127−8140.

https://doi.org/10.1021/acs.jpcc.3c00998
J. Phys. Chem. C 2023, 127, 8657−8669